Signatures of stabilization in the angle-resolved photoemission by an ultrashort intense XUV laser pulse

Wei-Chao Jiang,[1,*] Mu-Xue Wang,[2] Liang-You Peng,[2,3,†] and Joachim Burgdörfer[4]

[1]*College of Physics and Optoelectronic Engineering, Shenzhen University, Shenzhen 518060, China*

[2]*State Key Laboratory for Mesoscopic Physics and Frontiers Science Center for Nano-optoelectronics, School of Physics, Peking University, Beijing 100871, China*

[3]*Collaborative Innovation Center of Extreme Optics, Shanxi University, Taiyuan, Shanxi 030006, China*

[4]*Institute for Theoretical Physics, Vienna University of Technology, Wiedner Hauptstraße 8-10, A-1040 Vienna, Austria, European Union*

(Received 23 November 2021; accepted 20 January 2022; published 7 February 2022)

We explore features of stabilization in the angle-resolved spectra of photoelectrons when ground-state atomic hydrogen is exposed to an intense ($\sim 10^{18}$ W/cm^2) linearly polarized ultrashort XUV pulse. In this regime, atomic stabilization can be traced to the temporal destructive interference between wave packets released by the intense field at different instants of time. By a comparison between the numerical solution of the time-dependent Schrödinger equation and a semianalytical model, we can identify the observed oscillations in the momentum distribution and the suppression of photoemission into the laser polarization direction as a direct result of stabilization. We also explore the effect of nondipole corrections on the angular distribution.

DOI: 10.1103/PhysRevA.105.023104

I. INTRODUCTION

Atomic stabilization is a theoretically well-established strong-field effect that has been extensively studied for about 30 years. Accordingly, ionization is predicted to be significantly suppressed when the atom is exposed to a laser pulse with high intensities $I/I_0 \gg 1$ ($I_0 = 3.51 \times 10^{16}$ W/cm^2 is the characteristic intensity corresponding to a field strength of 1 a.u.) and high frequencies $\omega/E_0 \gg 1$ (E_0 is the binding energy of the atomic electron; ω is the energy or frequency of laser). This counterintuitive phenomenon clearly signifies the breakdown of perturbation theory, which predicts a monotonically increasing ionization rate as the laser intensity increases. The suppression of ionization in this highly nonperturbative radiation regime was first identified within the framework of the high-frequency Floquet theory (HFFT) in which a monochromatic plane wave corresponding to a pulse of infinite duration $T_p \to \infty$ is assumed [1–13]. The suppression mechanism in the high-frequency regime is frequently referred to as adiabatic stabilization.

Adiabatic stabilization can be conveniently viewed in the accelerated Kramers-Henneberger (KH) frame [14], in which the coordinate of the electron is transformed by $\mathbf{r} \to \mathbf{r} + \boldsymbol{\alpha}(t)$, with $\boldsymbol{\alpha}(t)$ being the classical time-dependent oscillatory quiver motion of a free electron in the laser field. In the KH frame, the atomic nucleus moves along the trajectory $-\boldsymbol{\alpha}(t)$, while the electron remains at rest. The electron-laser interaction appears now through an oscillating Coulomb potential $V_{\rm KH}(\mathbf{r}, t) = -1/[\mathbf{r} + \alpha(t)]$ (here and in the following we consider hydrogen). In a high-frequency Floquet expansion in ω^{-1}, the electron is, to zeroth order, exposed to the time-averaged KH potential $V_{\rm KH}(\mathbf{r}) = -1/T \int_0^T 1/[\mathbf{r} + \boldsymbol{\alpha}(t)]dt$, with T being the period of the laser field. With increasing peak field strength or intensity ($I = F_0^2$), the amplitude of the quiver motion of $\boldsymbol{\alpha}(t)$, $\alpha_0 = F_0/\omega^2 = I^{1/2}/\omega^2$, exceeds the atomic radius $a_0 = 1$ (in atomic units), and $V_{\rm KH}$ will evolve into a double well that can support infinitely many bound states. The electron density of the laser-dressed KH ground state will therefore evolve into a moleculelike two-peak distribution. Accordingly, stabilization results from the "dichotomy" of this electronic wave function which is located in the double well far away from the nucleus, thereby suppressing photoionization.

Experimental evidence for atomic stabilization has so far been restricted to atoms in Rydberg states [15–19]. Direct observation of adiabatic stabilization of ground-state atoms appears to be still missing. Recently, the search for verification of stabilization was reinvigorated by the remarkable experimental observation by Eichmann *et al.* [20], in which neutral atoms in an intense IR laser field were accelerated at an amazing high rate of 10^{15}m/s^2, sensitive to the existence of stable atoms in intense IR fields. Complementing the HFFT, stabilization was theoretically demonstrated also for finite pulses by numerically solving both the reduced-dimensional [21–24] and three-dimensional (3D) [25] time-dependent Schrödinger equation (TDSE). Exploring classical-quantum correspondence, it was found that atomic stabilization in 3D classical calculations requires much higher laser intensity than predicted by quantum theory [26].

The formation of dichotomic KH states suggests that stabilization could be monitored by the angle-resolved spectra of the photoelectron [27]. Moleculelike two-center interference fringes are predicted to be observable in a pump-probe scheme with orthogonal laser polarization [28]. The influence of

*jiang.wei.chao@szu.edu.cn
†liangyou.peng@pku.edu.cn

nondipole [29] and correlation [30,31] effects on stabilization was considered. Early studies based on reduced-dimensional TDSE calculations suggested the destruction of stabilization by either the nondipole effects [32] or the electron-correlation effects [33]. More recent full-dimensional TDSE calculations showed that the nondipole corrections can even enhance the stabilization instead of destructing it if a suitable pulse duration is chosen [34].

The aim of the present study is the exploration of signatures of stabilization in the angle-resolved photoelectron spectra (ARPES) of ground-state atoms, exposed to ultrashort (approximately femtosecond) XUV pulses with intensities of the order of 10^{18} W/cm^2 and photon energies of the order of 50–100 eV. Such pulses are expected to become available in free-electron laser (FEL) facilities [35–44] and, possibly, future high-intensity high-harmonics-generation (HHG) facilities. These pulses give access to an intermediate parameter regime of competing length and energy scales in which a complex array of physical processes is expected to contribute. The quiver amplitude α_0 becomes comparable to the atomic radius, $\alpha_0 \sim 1$, but is not yet large enough to generate a pronounced dichotomy of the wave function. The photon energy exceeds the atomic binding energy, $\omega/E_0 \gtrsim 4$, but is not sufficiently large that the asymptotic high-frequency theory would apply. Furthermore, the multicycle pulse duration of the order of 10 optical cycles results in a strong influence of the temporal shape of the pulse envelope while, at the same time, some features of the constant-field Floquet theory of adiabatic stabilization remain approximately preserved.

We compare our numerically accurate solutions of the TDSE with a simple semianalytical model which provides an intuitive picture of stabilization for this intermediate parameter regime that is complementary to the asymptotic high-field stabilization scenario of dichotomy. Stabilization is found to be the consequence of a destructive temporal interference between wave packets emitted at different instants of time. The key parameter controlling the interference phase is identified to be $\alpha_0 k_z$, where k_z is the momentum component along the laser polarization direction. The closely related parameter $\alpha_0 k_y$ (k_y is the momentum component along the laser propagation direction), in turn, controls the influence of nondipole effects, which we also consider. The focus of the present work is on the angular distribution of photoemission and on the identification of signatures of the onset of stabilization.

This paper is organized as follows: In Sec. II, we briefly review our approach to numerically solve the TDSE for a one-electron atom in a strong multicycle XUV field. A semianalytical model accounting for the stabilization by destructive interference and the angular distribution of the emitted electron is presented in Sec. III. Following the discussion of numerical results in Sec. IV, a brief summary is given in Sec. V. Unless stated otherwise, atomic units are used.

II. SOLUTION OF THE TIME-DEPENDENT SCHRÖDINGER EQUATION

The TDSE governing the time evolution of a hydrogenic state in the presence of an intense XUV field is given in the laboratory frame by

$$i\frac{\partial}{\partial t}\Psi(\mathbf{r},t) = \left(-\frac{1}{2}\nabla^2 - \frac{1}{r} + H_{\rm I}\right)\Psi(\mathbf{r},t). \tag{1}$$

The form of the interaction Hamiltonian $H_{\rm I}$ depends on both the chosen gauge and the inclusion of magnetic field effects. In the velocity (V) gauge of the (electric) dipole (d) approximation, the time-dependent interaction Hamiltonian $H_{\rm I}$ between the electron and the laser field is given by

$$H_{\rm I}^{\rm d,V} = -i\frac{1}{c}\mathbf{A}(t)\cdot\boldsymbol{\nabla}, \tag{2}$$

and in the length (L) gauge it is given by

$$H_{\rm I}^{\rm d,L} = \mathbf{r}\cdot\mathbf{F}(t), \tag{3}$$

where $\mathbf{A}(t)$ and $\mathbf{F}(t) = -(1/c)d\mathbf{A}/dt$ are the vector potential and the electric field of the pulse, respectively. For weak fields, the validity of the dipole approximation depends on the smallness of the photon wave number $\xi_p = \omega/c \ll 1$ of the radiation on the atomic scale, which is well satisfied for the frequencies ω of XUV pulses. For intense pulses, however, in addition the quiver velocity $\omega\alpha_0$ is required to be small compared to the speed of light $\omega\alpha_0/c \ll 1$. Therefore, with increasing intensity and frequency nondipole corrections may become non-negligible. We take into account the first-order nondipole correction in our TDSE calculations, for which we use two alternative expressions. One is given by [45–49]

$$\begin{aligned} H_{\rm I}^{\rm Nd1} = &-i\frac{1}{c}\mathbf{A}(t)\cdot\boldsymbol{\nabla} + \frac{1}{c^2}(\hat{k}\cdot\mathbf{r})[\mathbf{F}(t)\cdot\mathbf{A}(t)] \\ &-i\frac{1}{c}(\hat{k}\cdot\mathbf{r})[\mathbf{F}(t)\cdot\boldsymbol{\nabla}], \end{aligned} \tag{4}$$

with $\hat{k}$ representing the propagation direction of the laser pulse. Throughout this paper, we choose the propagation direction to be along the y axis and the polarization direction to be along the z axis. We have also implemented an alternative form in the so-called propagation gauge [50],

$$H_{\rm I}^{\rm Nd2} = -i\frac{1}{c}\mathbf{A}(t)\cdot\boldsymbol{\nabla} - i\frac{A^2(t)}{2c^3}\hat{k}\cdot\boldsymbol{\nabla}. \tag{5}$$

The nondipole correction breaks the axial symmetry of the system. As a consequence, the excitations of states with a nonzero magnetic quantum number make the numerical calculations much more challenging than in the dipole approximation.

In our simulation, we use, for the time dependence of the vector potential $\mathbf{A}(t) = A(t)\hat{z}$,

$$A(t) = A_0 g(t)\sin(\omega t), \tag{6}$$

with a Gaussian envelope,

$$g(t) = \exp(-t^2/T^2). \tag{7}$$

The FWHM $T_{\rm FWHM}$ of the pulse is related to the parameter T in Eq. (7) by $T_{\rm FWHM} = \sqrt{2\ln 2}\,T$. The classical displacement of a free electron exposed to the laser field with vector potential $A(t)$, referred to as quiver motion, is given by

$$\alpha(t) = \frac{1}{c}\int_{t_0}^{t} A(\tau)d\tau. \tag{8}$$

For a sufficiently long pulse, $\alpha(t)$ can be approximated by

$$\alpha(t) \approx -\alpha_0 g(t)\cos(\omega t), \tag{9}$$

with peak quiver amplitude

$$\alpha_0 = \frac{A_0}{c\omega}. \tag{10}$$

The amplitude of $\alpha(t)$, $\alpha_0 g(t)$, is the key parameter relating the present TDSE results to those from Floquet theory. It determines if and when the ionization dynamics enters into the adiabatic stabilization regime.

We have checked on the gauge independence of our numerical results. For the two dipole gauges [Eqs. (2) and (3)] we find (nearly) identical results within our numerical accuracy. In the following calculations, we employ the velocity gauge [Eq. (2)] since only a much smaller range of angular momenta is required for convergence. Comparing numerical results based on the two nondipole forms $H_{\rm I}^{\rm Nd1}$ and $H_{\rm I}^{\rm Nd2}$ [Eqs. (4) and (5)], we find reasonably close agreement (see Sec. IV), although the calculation using $H_{\rm I}^{\rm Nd2}$ is found to converge faster for the present system.

A detailed description of the present method to numerically solve the TDSE can be found in Ref. [51]. In brief, we expand the wave function of the electron in terms of spherical harmonics. The radial wave function is discretized by the finite-element discrete-variable representation method [52–54]. The wave-function splitting method [55] is employed to avoid the need for large computational boxes. The photoelectron wave function is repeatedly divided into the inner part and the exterior part. The inner part is propagated by the full TDSE, while the exterior part is propagated analytically by neglecting the influence of the Coulomb potential. This numerical scheme for the TDSE was used previously to study the dynamic interference [56], harmonic generation [57], and dynamically enhanced Autler-Townes splittings [58].

III. SEMI-ANALYTICAL MODEL

In this section, we present a simple semianalytical model based on first-order distorted-wave theory which provides insights into the origin of stabilization in the regime of moderately intense XUV pulses, complementing the picture of adiabatic stabilization in the high-field regime. Moreover, it yields predictions for the angular distribution in closed form and allows us to estimate the influence of nondipole contributions.

A. Stabilization by destructive temporal interference

For moderately strong XUV fields one-photon transitions to the continuum still dominate over multiphoton ionization. Therefore, the differential change in the photoelectron amplitude is in the dipole approximation given by

$$da_{\mathbf{k}}(t) = -\frac{1}{c}\exp\left[-i\Phi(t,\tau)\right]\langle\psi_{\mathbf{k}}|\frac{\partial}{\partial z}|\psi_0\rangle a_0(\tau)A(\tau)d\tau, \tag{11}$$

where $|\psi_0\rangle$ is the initial ground state with energy $E_0 = -0.5$ a.u., $|\psi_{\mathbf{k}}\rangle$ is the final scattering state with asymptotic momentum $\mathbf{k}$, and $a_0(\tau)$ is the amplitude of the initial state at τ. The influence of the strong XUV field is accounted for nonperturbatively in terms of a Volkov phase,

$$\begin{aligned}\Phi(t,\tau) &= \int_\tau^t \left[\frac{k^2}{2} + \frac{1}{c}k_z A(\tau')\right]d\tau', \\ &= \frac{k^2}{2}(t-\tau) + k_z[\alpha(t)-\alpha(\tau)].\end{aligned} \tag{12}$$

Integrating the differential ionizing amplitudes [Eq. (11)] from the initial time t_0 to a given time t yields the cumulative amplitude at t,

$$a_{\mathbf{k}}(t) = -\frac{1}{c}\langle\psi_{\mathbf{k}}|\frac{\partial}{\partial z}|\psi_0\rangle\int_{t_0}^t a_0(\tau)A(\tau)\exp[-i(\Phi(t,\tau))]d\tau. \tag{13}$$

Utilizing the substitution

$$\Phi(t,\tau) = \Phi(t,t_0) - \Phi(\tau,t_0), \tag{14}$$

Eq. (13) can be rewritten as

$$\begin{aligned}a_{\mathbf{k}}(t) = &-\frac{1}{c}\exp[-i\Phi(t,t_0)]\langle\psi_{\mathbf{k}}|\frac{\partial}{\partial z}|\psi_0\rangle \\ &\times\int_{t_0}^t a_0(\tau)A(\tau)\exp[i(\Phi(\tau,t_0))]d\tau.\end{aligned} \tag{15}$$

Equation (15) can be viewed as a variant of a first-order distorted-wave approximation. While the (one-)photon absorption process is described in first order, initial and final states involved in the transition account for effects beyond first order. Strong-field effects are included in Eq. (15) through both the Volkov phase (12) of the final state and the complex ground-state amplitude $a_0(\tau)$ of the initial state. The latter accounts for both the energy shift and the depletion by the strong field. Conversely, if $a_0(\tau)$ were replaced by the field-free amplitude $a_0(\tau) = \exp(-iE_0\tau)$ and the Volkov phase were deleted, the conventional transition amplitude in first-order perturbation theory would be recovered.

The occupation amplitude $a_0(\tau)$ accounts for the depletion of population as well as the phase shift of the initial state due to the ac Stark shift,

$$a_0(\tau) = f(\tau)\exp\left[-i\left(E_0\tau + \int_{t_0}^\tau \delta E_0(\tau')d\tau'\right)\right], \tag{16}$$

with $f(\tau)$ being the modulus of $a_0(\tau)$ and $\delta E_0(\tau)$ being the instantaneous energy shift induced by the XUV pulse oscillating with twice the frequency ω of the XUV field. The cycle-averaged value of the ac Stark shift

$$\delta\bar{E}_0(t) = \frac{\omega}{2\pi}\int_{-\frac{\pi}{\omega}+t}^{\frac{\pi}{\omega}+t}\delta E_0(t')dt' \tag{17}$$

follows the temporal evolution of the envelope of the pulse, is a monotonically increasing function with instantaneous laser intensity, and is responsible for the appearance of the dynamic interference [56,59–67] in the photoelectron energy spectra. Equation (17) also allows for a comparison with the HFFT [4], which assumes a constant field amplitude. The resulting time-independent ac Stark shift calculated for a parametrically varied intensity agrees quite well with the TDSE result for the time-varying envelope (Fig. 1). This indicates that a short

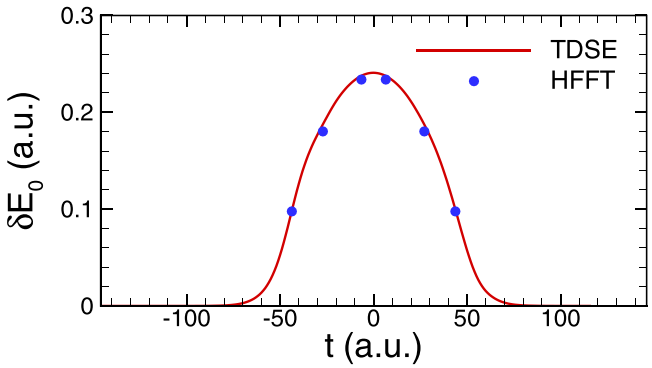

FIG. 1. The time-dependent ac Stark energy shift of the ground-state H atom in the laser pulse with a peak intensity of 5×10^{18} W/cm^2, photon energy of 53.6 eV, and pulse length T of 1 fs. The present TDSE calculation is compared with the high-frequency Floquet theory (HFFT) [4]. To facilitate the comparison, the instantaneous laser intensity of the pulse at time t is used as the constant intensity in the HFFT.

pulse with a length of the order of 10 optical cycles is already sufficiently long to reproduce features of HFFT. Analogously to Eq. (17), we consider a cycle-averaged modulus of the occupation amplitude

$$\bar{f}(t) = \frac{\omega}{2\pi}\int_{-\frac{\pi}{\omega}+t}^{\frac{\pi}{\omega}+t} f(t')dt', \tag{18}$$

which describes the cycle-averaged depletion of the initial state during the rise and fall of the XUV pulse. For the numerical results presented in the following, we take both $\bar{f}(t)$ and $\delta\bar{E}_0(t)$, for reasons of accuracy, directly from the TDSE calculations run in parallel by projecting the time-dependent wave function onto the initial ground state. However, as demonstrated previously [56,64], this input can alternatively be determined from lowest-order perturbation theory for the energy shift and the decay rate of the initial state.

By expressing the vector potential of the pulse as

$$A(t) = \frac{i}{2}A_0 g(t)\exp(-i\omega t) - \frac{i}{2}A_0 g(t)\exp(i\omega t), \tag{19}$$

Eq. (15) can be rewritten in the rotating-wave approximation (RWA) as

$$a_{\mathbf{k}}(t) = -\frac{iA_0}{2c}e^{-i[\Phi(t,t_0)+\phi_V(t_0)]}\langle\psi_{\mathbf{k}}|\frac{\partial}{\partial z}|\psi_0\rangle \times \int_{t_0}^{t} f(\tau)g(\tau)e^{i[(E_{k0}-\omega)\tau+\phi_S(\tau)+\phi_V(\tau)]}d\tau, \tag{20}$$

with the zero-field excitation energy

$$E_{k0} \equiv \frac{k^2}{2} - E_0, \tag{21}$$

the Stark-shift phase

$$\phi_S(\tau) \equiv \int_{t_0}^{\tau} -\delta E_0(\tau')d\tau', \tag{22}$$

and the contribution from the Volkov phase

$$\phi_V(\tau) \equiv k_z\alpha(\tau). \tag{23}$$

The RWA is applicable since the rapidly oscillating phase $(E_{k0}+\omega)\tau$ [Eq. (20)] from the counterrotating term would yield a negligible contribution.

The rapidly varying phase (23) plays the key role in suppressing ionization. Using Euler's formula

$$\exp[i\phi_V(\tau)] = \cos[\phi_V(\tau)] + i\sin[\phi_V(\tau)], \tag{24}$$

Eq. (20) can be approximated by

$$a_{\mathbf{k}}(t) \approx -\frac{iA_0}{2c}e^{-i[\Phi(t,t_0)+\phi_V(t_0)]}\langle\psi_{\mathbf{k}}|\frac{\partial}{\partial z}|\psi_0\rangle\int_{t_0}^{t}\cos[\phi_V(\tau)] \times f(\tau)g(\tau)e^{i[(E_{k0}-\omega)\tau+\phi_S(\tau)]}d\tau, \tag{25}$$

exploiting the fact that the rapidly varying phase $\phi_V(\tau)$ leads to equally likely positive and negative values, thereby suppressing the contribution from the sine term.

Resonant transitions to a given continuum state with final energy $E = k^2/2$ occur near stationary points of the phase in the integrand of Eq. (25), given by

$$E_{k0} - \omega - \delta E_0(\tau) = 0. \tag{26}$$

The strength of the transition is modulated by the $\cos[\phi_V(\tau)]$ prefactor. When $k_z\alpha_0$ in the oscillating phase $\phi_V(\tau)$ is smaller than $\pi/2$, $\cos[\phi_V(\tau)]$ is confined to the interval $[\cos(k_z\alpha_0), 1]$ for all τ and is positive for near-resonant transitions [Eq. (26)]. Therefore, different portions of the wave packet emitted in the interval $[t_0, t]$ will constructively interfere. However, as soon as $k_z\alpha_0$ exceeds $\pi/2$, $\cos[\phi_V(\tau)]$ may change sign, and destructive temporal interference will set in. The suppression of ionization by destructive temporal interference is illustrated in Fig. 2 for two different momenta (or, equivalently, photoelectron energies $E = k^2/2$). Due to the time-dependent ac Stark shift, the photoelectron ejected after absorption of one photon at different instants of time will have different final energies. Early and late in the temporal wings of the pulse the energy shift is small (e.g., $k = 1.78$ a.u. in the present case), while larger energies are reached near the peak of the pulse. At the time when the $k = 1.83$ a.u. electron is ejected, the amplitude of the phase $k_z\alpha_0$ reaches almost π, and $\cos[\phi_V(\tau)]$ oscillates between -1 and 1. The temporal interference is destructive, the ionization amplitude (25) nearly vanishes, and stabilization sets in [Fig. 2(a1)]. By contrast, for $k = 1.78$ a.u. the amplitude is close to $\pi/2$. Thus, nearly all the values of $\cos[\phi_V(\tau)]$ are positive, destructive temporal interference is absent [Fig. 2(a2)], and no significant stabilization is expected (see also below).

The resulting angular-differential ionization probability is calculated according to

$$P_{\mathbf{k}} = |a_{\mathbf{k}}|^2, \tag{27}$$

with the amplitude $a_{\mathbf{k}}$ given by Eq. (25). The photoelectron energy spectrum is derived from $P_{\mathbf{k}}$ by integrating over all emission angles,

$$P(E) = \int_0^{\pi}\int_0^{2\pi} P_{\mathbf{k}}k\sin\theta d\phi d\theta, \tag{28}$$

with $E = k^2/2$.

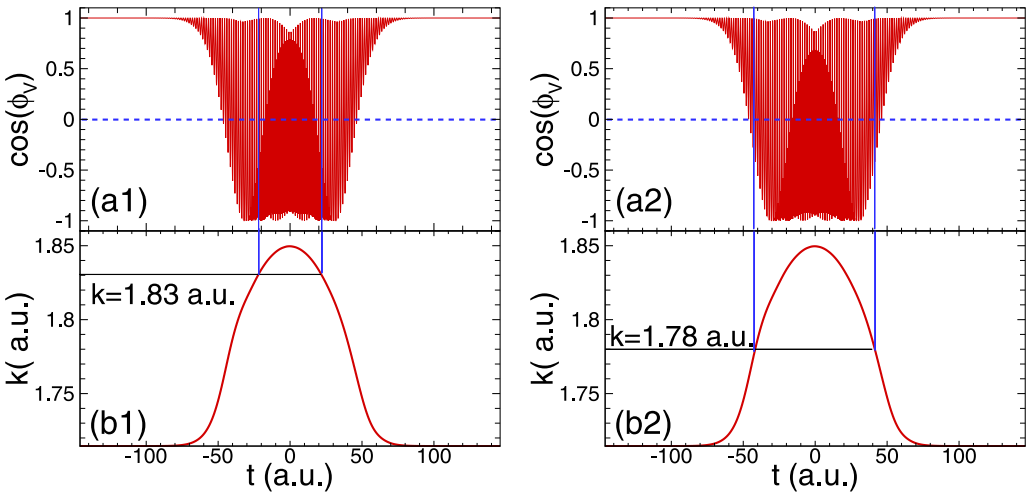

FIG. 2. Volkov phase ϕ_V [Eq. (23)] as a function of time for the Gaussian envelope of the pulse (same as in Fig. 1). Vertical blue lines mark the instants when the resonant transitions to the final state with (a1) and (b1) momentum $k = 1.83$ a.u. and (a2) and (b2) $k = 1.78$ a.u. occur. (a1) and (a2) Displayed is $\cos[\phi_V(t)]$. In (a1), $\cos[\phi_V(t)]$ rapidly varies between -1 and $+1$ in the vicinity of the vertical blue line. In (a2), $\cos[\phi_V(t)]$ is predominately positive.

B. Angular distribution of photoemission in dipole approximation

Starting from Eq. (20), we first derive a simple estimate for the angular distribution of the photoelectron in the stabilization regime for moderately strong XUV fields in dipole approximation. We consider the contribution to ionization from a single cycle at time $t = t_c$, during which we assume the envelope function $g(t) \approx g(t_c)$ is constant, thereby involving the adiabatic approximation. Accordingly, the contribution to the ionization amplitude from this cycle is

$$a_{\mathbf{k}}(t_c) = N\langle\psi_{\mathbf{k}}|\frac{\partial}{\partial z}|\psi_0\rangle \times \int_{t_c-\frac{\pi}{\omega}}^{t_c+\frac{\pi}{\omega}} f(\tau)\beta(\tau)e^{i[k_z\alpha_0 g(t_c)\cos(\omega\tau)]}d\tau, \quad (29)$$

where $\beta(\tau)$ is short for

$$\beta(\tau) = \exp\left[i(E_{k0}-\omega)\tau + \int_{-\frac{\pi}{\omega}+t_c}^{\tau'} \delta E_0(\tau')d\tau'\right] \quad (30)$$

and N is short for the prefactors

$$N = -\frac{iA_0}{2c}e^{-i[\Phi(t_c+\frac{\pi}{\omega},t_c-\frac{\pi}{\omega})+\phi_V(t_c-\frac{\pi}{\omega})]}. \quad (31)$$

Both the modulus of the ground-state amplitude $f(t)$ and the energy shift $\delta E_0(t)$ will, in general, strongly vary within a cycle following the laser field oscillation for strong field. For moderate intensities, the variation of both $f(t)$ and $\delta E_0(t)$ is small, and in this regime these quantities can be replaced by the cycle average $\bar{f}(t_c)$ [Eq. (18)] and $\delta\bar{E}_0(t_c)$ [Eq. (17)]. We note that in the regime of very high intensities for which alternative predictions for angular distributions are available [9,13], this approximation may break down. Near the stationary point of resonant transitions to the continuum, the one-cycle contribution to the ionization amplitude becomes

$$a^c_{\mathbf{k}}(t_c) = N\bar{f}(t_c)\langle\psi_{\mathbf{k}}|\frac{\partial}{\partial z}|\psi_0\rangle\int_{-\frac{\pi}{\omega}}^{\frac{\pi}{\omega}} e^{i[k_z\alpha_0 g(t_c)\cos(\omega\tau)]}d\tau. \quad (32)$$

The time integral in Eq. (32) can be expressed in terms of the Bessel function of the first kind J_0,

$$a^c_{\mathbf{k}}(t_c) = \frac{2\pi}{\omega}N\bar{f}(t_c)\langle\psi_{\mathbf{k}}|\frac{\partial}{\partial z}|\psi_0\rangle J_0(k_z\alpha_0 g(t_c)). \quad (33)$$

The dipole transition matrix element can be factorized into the radial part $d(k)$ and the angular part $\cos\theta$,

$$\langle\psi_{\mathbf{k}}|\frac{\partial}{\partial z}|\psi_0\rangle = d(k)\cos\theta, \quad (34)$$

where the radial part is given for hydrogenic wave functions by

$$d(k) = \frac{\sqrt{2}k}{3\pi}ie^{\pi/2k}\Gamma(2-i/k) \times \int_0^\infty r^3 e^{-r-ikr}\,{}_1F_1(2+i/k,4,2ikr)dr \quad (35)$$

with Γ being the gamma function and ${}_1F_1$ being the Kummer confluent hypergeometric function. Using Eq. (34), we obtain the photoelectron angular distribution in the strong field as

$$\left|a^c_{\mathbf{k}}\right|^2 = M(k)\cos^2\theta J_0^2(k\alpha_0 g(t_c)\cos\theta), \quad (36)$$

with the angle-independent factor $M(k)$ given by

$$M(k) = \frac{2\pi}{\omega}N\bar{f}(t_c)d(k). \quad (37)$$

When $k_z\alpha_0 g(t_c) \ll 1$, Eq. (36) converges to the well-known perturbative distribution $\propto\cos^2\theta$. When $k_z\alpha_0 g(t_c) \gg 1$, the Bessel function $J_0(x)$ can be approximated by its asymptotic limit for large arguments

$$J_0(x) \underset{x\to\infty}{\approx} \sqrt{\frac{2}{\pi x}}\cos\left(x-\frac{\pi}{4}\right), \quad (38)$$

and Eq. (36) yields

$$\left|a_{\mathbf{k}}^{c}\right|^{2} \approx \frac{2M(k)|\cos\theta|}{\pi k\alpha_0 g(t_c)} \cos^2\left(|k\alpha_0 g(t_c)\cos\theta| - \frac{\pi}{4}\right). \quad (39)$$

We note that the present angular distribution differs from that predicted for the high-frequency high-field limit given by [9,13]

$$\frac{d\Gamma}{d\Omega} = \frac{8|\psi_0^d(\alpha_0 g(t_c)\hat{z})|^2}{\pi k^3} \frac{\cos^2\left[|k\alpha_0 g(t_c)\cos\theta| + \frac{\pi}{4}\right]}{|\alpha_0 g(t_c) k\cos\theta|}, \quad (40)$$

which is valid for $\alpha_0 g(t_c) k\cos\theta \gg 1$. The function $\psi_0^d(\alpha_0 g(t_c)\hat{z})$ represents the wave function of the dressed state of the initial state. It should be emphasized that the applicability of Eq. (40) does not extend to the intermediate-field regime addressed in the present paper. A qualitative comparison between Eqs. (39) and (40) will be presented below [see Fig. 6(a)].

C. The nondipole correction of the angular distributions

We consider the nondipole correction of the angular distribution within our model by reexpressing the phase ϕ_V in Eq. (20) as [10,48]

$$\phi_V(\tau) = k_z\alpha(\tau) + \phi^{\mathrm{ND}}(\tau), \quad (41)$$

with

$$\phi^{\mathrm{ND}}(\tau) = \frac{k_y k_z}{c}\alpha(\tau) + \frac{k_y}{2c^3}\int_{t_0}^{\tau} A^2(\tau')d\tau' \quad (42)$$

derived from the nondipole correction of the Volkov state. Obviously, the correction (42) does not change the photoelectron distribution in the x-z plane, the plane perpendicular to the laser propagation direction $\hat{y}$, since $\phi^{\mathrm{ND}}(\tau) = 0$ for $k_y = 0$. However, it will modify the photoelectron distribution in planes containing the propagation direction, e.g., in the y-z plane.

Inserting the explicit expression of the vector potential (6) into Eq. (42), we find

$$\phi^{\mathrm{ND}}(\tau) = \frac{k_y k_z}{c}\alpha(\tau) + \frac{k_y A_0^2}{4c^3}\int_{t_0}^{\tau} g^2(\tau')[1-\cos(2\omega\tau')]d\tau'. \quad (43)$$

The second term in Eq. (43) provides the nondipole correction to the cycle-averaged ac Stark shift

$$\delta\bar{E}^{\mathrm{ND}}(\tau) = \frac{k_y A_0^2}{4c^3} g^2(\tau). \quad (44)$$

It depends on the direction of emission either raising (for $k_y > 0$) or lowering (for $k_y < 0$) the effective ionization potential. Consequently, the electrons ejected in different directions may have different energies even if they are experiencing the same instantaneous laser intensity.

In the pulsed laser field, the photoelectron distribution in the y-z plane is influenced not only by the instantaneous nondipole ac Stark shift but also by the phase difference between the two photoelectron wave packets ejected at the rising and falling edges of the pulse. The portion of the electronic wave packet ejected at the rising edge will acquire an additional phase shift $\Delta\phi^{\mathrm{ND}}$ in the peak field prior to the ejection of the corresponding portion on the falling edge. The resulting phase difference contributes to the nondipole correction. This phase difference can be expressed as

$$\Delta\phi = \Delta\phi_0 - \Delta\phi^{\mathrm{ND}}, \quad (45)$$

where $\Delta\phi_0$ is the corresponding phase difference in the dipole approximation [56]

$$\Delta\phi_0 = \int_{t_1}^{t_2} [\delta E_0(\tau) - \delta E_0(t_1)]d\tau + \frac{\pi}{2}, \quad (46)$$

with t_1 and t_2 ($t_1 = -t_2$) being the ejection times of two electron wave packets. $\Delta\phi^{\mathrm{ND}}$ is the nondipole phase accumulated between t_1 and t_2,

$$\Delta\phi^{\mathrm{ND}} = \int_{t_1}^{t_2} \delta E^{\mathrm{ND}}(\tau)d\tau = \frac{k_y A_0^2}{4c^3}\int_{t_1}^{t_2} g^2(\tau)d\tau. \quad (47)$$

The ejection times t_1 and t_2 depend not only on the energies of the photoelectrons but also on their ejection directions because of the angle dependence of the ac Stark shift of the nondipole correction [Eq. (44)]. This fact makes it difficult to find a simple analytical expression for the nondipole angular distribution of the photoelectron at fixed energy, in analogy to Eq. (36). However, the angle dependence of t_1 and t_2 becomes negligible for the electrons ejected during tails of the pulse because the corresponding ac Stark shifts are small. The nondipole phase (47) between the two electron wave packets ejected in the tails can be well approximated by taking the limit $-t_1 = t_2 \to \infty$,

$$\Delta\phi^{\mathrm{ND}}(t_2 \to \infty) = \frac{\sqrt{2\pi}kA_0^2 T}{8c^3}\sin\theta\sin\varphi \quad (48)$$

for a Gaussian envelope of the pulse (7). With the help of Eqs. (45) and (48), we find a simple analytical angular distribution in this limit as

$$P_{\mathbf{k}}(t_2 \to \infty) \propto \cos^2\theta|1 + se^{i\Delta\phi}|^2 = \cos^2\theta\left[1 + s^2 + 2s\cos\left(\Delta\phi_0 - \frac{\sqrt{2\pi}kA_0^2 T}{8c^3}\sin\theta\sin\varphi\right)\right], \quad (49)$$

where $s = \bar{f}(t_2)/\bar{f}(t_1)$ ($t_2 \to \infty$) is the ratio of the probability amplitude of the two interfering electron wave packets which can be obtained from the surviving ground-state population after the pulse.

IV. COMPARISON BETWEEN TDSE AND THE SEMI-ANALYTICAL MODEL

In the following we present numerical results for ARPES of hydrogen using an XUV pulse with intensities of 10^{18}

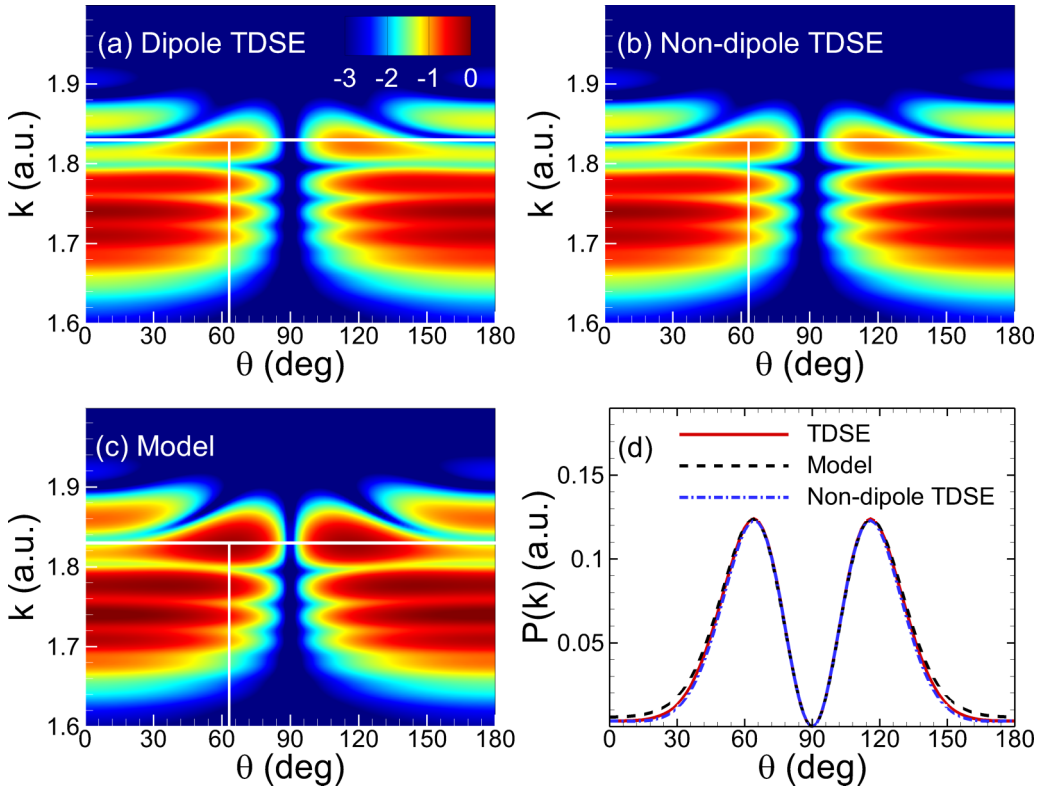

FIG. 3. Momentum spectrum of the photoelectron. The laser parameters are the same as in Fig. 1. Predictions from (a) dipole TDSE, (b) nondipole TDSE, and (c) the dipole model are shown. The horizontal white lines in (a)–(c) mark the momentum $k = 1.83$ a.u., and $P(k)$ along this cut is shown in (d). The model result in (d) has been rescaled to match the TDSE results. Along the vertical solid lines in (a)–(c), the oscillations due to dynamic interference are visible.

to 10^{19} W/cm^2, pulse duration T of 1 to 2 fs, and photon energies of 30–100 eV and compare these results with the predictions by the semianalytical model outlined in the previous section. We present two-dimensional distributions as a function of the polar angle θ relative to the polarization axis and the wave number $k = \sqrt{2E}$ of the ejected electron and project onto two planes: the x-z plane (azimuthal angle $\phi = 0$) perpendicular to the laser propagation and the y-z plane ($\phi = \pi/2$) spanned by the laser polarization and propagation vectors.

For the distribution in the plane perpendicular to the propagation direction [Figs. 3(a)–3(c)], we find close agreement between the TDSE solutions in the dipole approximation [Fig. 3(a)] and the nondipole correction [Fig. 3(b)] as well as the dipole limit of the semianalytical model [Fig. 3(c)]. The close agreement between the dipole and nondipole solutions was to be expected as significant nondipole contributions appear only along the propagation direction [Eq. (42)]. For vertical cuts at fixed θ (e.g., 63° in Fig. 3), the emission probabilities as a function of k (or E) display oscillations as a function of k signifying the temporal dynamical interference between the wave packets emitted during the rising and falling edges of the pulse reaching the same final state (k). The appearance of these oscillations was found to be a signature of the onset of stabilization [56,66] because significant emission on the falling edge is possible only after the onset of stabilization suppressing ionization in the peak field. Stabilization can now also be observed as a function of θ at fixed k (or E) along the horizontal line, e.g., $k = 1.83$ a.u. in Fig. 3(a). The probability density $P(\mathbf{k})$ along this cut is shown in Fig. 3(d). The angular distribution dramatically deviates from a $\cos^2\theta$ distribution and features a pronounced maximum near $\theta \approx 63°$. This anomalous distribution is found only for large k (or E) within the spectral width of the one-photon emission line, while at smaller k (e.g., near $k = 1.7$) a conventional $\cos^2\theta$ distribution prevails. At low k, the ac Stark shift is still small, indicating emission at the front or tail end of the pulse. Consequently, at such small instantaneous intensities the predictions of perturbation theory for the angular distribution still apply. By contrast, emission of electrons with higher energy corresponding to large ac Stark shifts occurs near the peak of the pulse where stabilization is operational. Here, perturbation theory breaks down, and the angular distribution peaks near $\theta = 63°$. The semianalytical model based on distorted-wave theory [Eq. (25)] predicts the numerical angular distribution quite well [Fig. 3(d)].

The destructive interference structure and thus the angular distribution in the stabilization regime are controlled by the cycle-averaged quiver phase $k_z\alpha_0 g(t_c)$, the product of the wave number and mean quiver amplitude (or intensity) for a given cycle t_c, shown in Fig. 4 in the k-θ plane. For low k, small phases can be found near $\theta = 0$, preserving the dipole emission pattern. With increasing k the region of small interference phases ($<\pi/2$) shifts to larger angles, resulting in a peak near

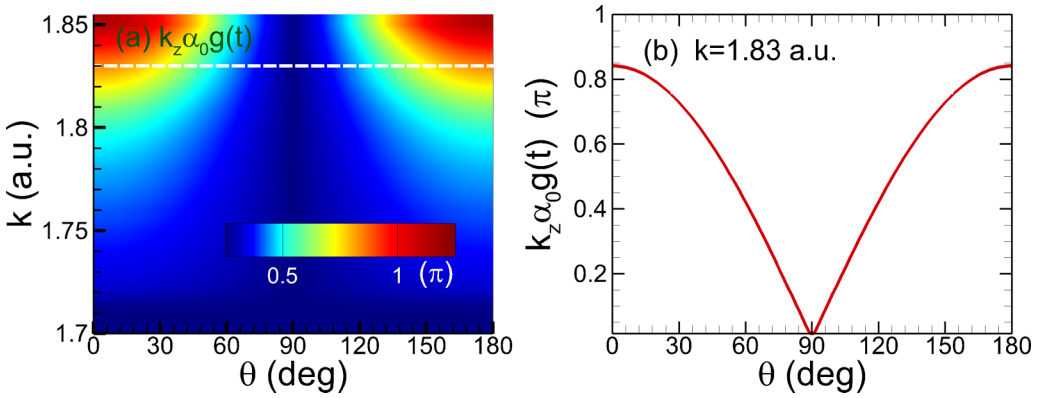

FIG. 4. (a) The amplitude $k_z\alpha_0 g(t)$ of the Volkov phase ϕ_V [Eq. (23)] of the photoelectron as a function of k and θ with the quiver amplitude α_0 given at the instant of the ionization. (b) The cut along the line at $k = 1.83$ a.u. in (a). The laser pulse is the same as in Fig. 1.

$\theta = 63^\circ$ at $k = 1.83$ a.u. [the cut along this line is shown in Fig. 4(b)].

The interplay between dynamical interference due to the temporal double slit and the destructive interference by large values of the cycle-averaged quiver phase is illustrated in Fig. 5 for the angular-differential emission $P(k, \theta = 0)$ along the laser polarization direction. The periodic oscillations on top of a smooth background are due to the interference between emissions on the rising (t_1) and falling (t_2) edges of the pulse. The strong suppression of and even vanishing emission at high values of k marked by an arrow is, however, the result of the global destructive interference due to the quiver phase [Fig. 5(a)] and a clear hallmark of stabilization. Omitting this phase from the semianalytical model, which is also shown in Fig. 5(a), leaves the double-slit oscillations qualitatively intact while increasing their amplitude for large k. The suppression of the emission for large k is, however, missing. In fact, the near-zero emission probability is replaced by a maximum. The minimum due to stabilization interference is predicted, according to Eq. (36), to occur when $\alpha_0 k_z g(t) = 2.4$ [the zero of the Bessel function J_0, marked by a blue circle in Fig. 5(b)], which is slightly lower than the actual position $\alpha_0 k_z g(t) = 2.7$

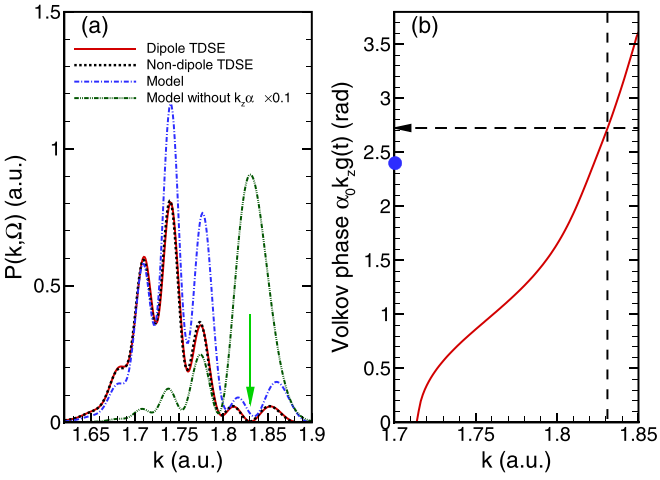

FIG. 5. (a) Photoelectron momentum spectra in the forward direction $P(k, \theta = 0)$. The green arrow marks the region of stabilization by destructive interference. The simplified model (when $k_z\alpha$ is dropped) neglecting destructive interference has been rescaled by a factor 1/10. (b) The amplitude $\alpha_0 k_z$ of the Volkov phase as a function of photoelectron momentum at fixed ejection angle $\theta = 0$. The black arrow marks the Volkov phase of the destructive interference, and the blue circle marks the prediction by Eq. (36). The laser pulse is the same as in Fig. 1.

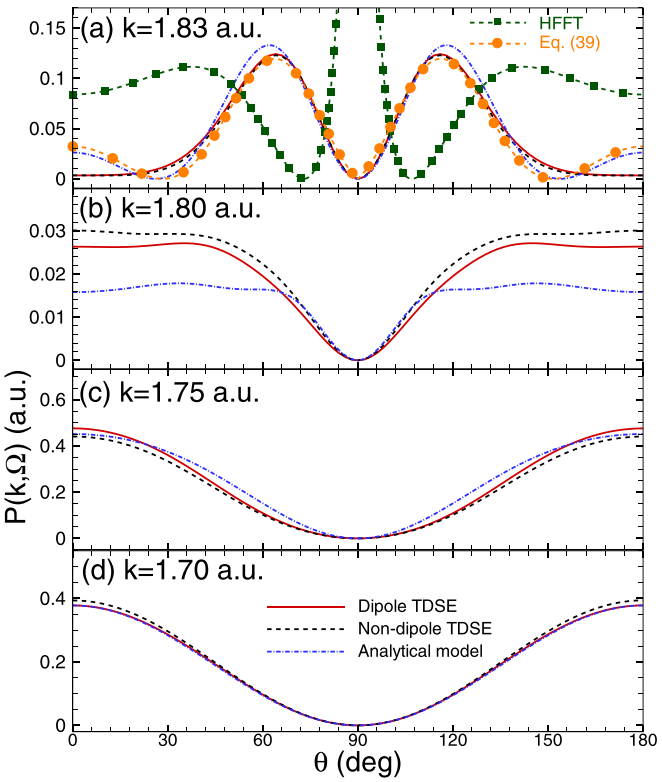

FIG. 6. The angular distribution in the x-z plane at fixed photoelectron momentum magnitude (a) $k = 1.83$ a.u., (b) $k = 1.80$ a.u., (c) $k = 1.75$ a.u., and (d) $k = 1.70$ a.u. The TDSE results with and without the nondipole correction are compared with the analytical estimate [Eq. (36)]. In (a), the asymptotic solutions for large $k_z\alpha$ of Pont [9] within HFFT [Eq. (40)] and of the present analytical estimates (36) and (39) are also given. The laser pulse is the same as in Fig. 1.

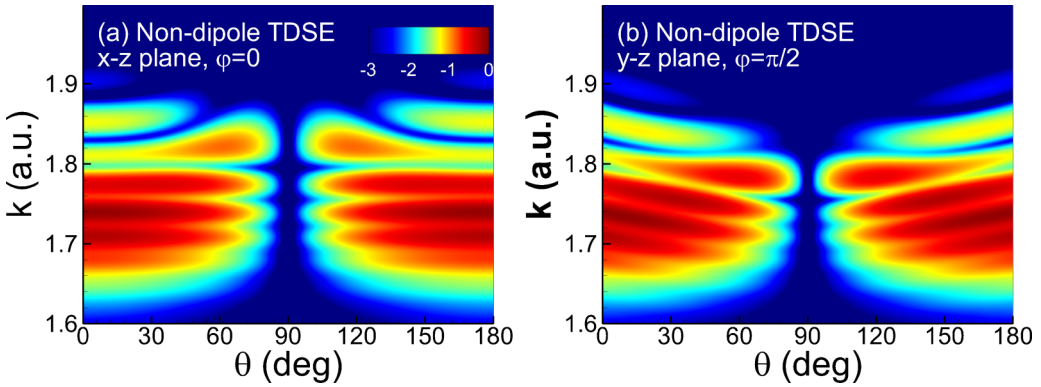

FIG. 7. Photoelectron momentum spectra in (a) the x-z plane and (b) the x-y plane with the nondipole corrections included. The propagation direction and the polarization direction of the laser pulse are along the y axis and the z axis, respectively. The laser pulse is the same as in Fig. 1.

[marked by a black arrow in Fig. 5(b)]. This difference can be viewed as a signature of nonadiabatic effects.

The angular distribution in the x-z plane for fixed k (Fig. 6) confirms the near-perfect agreement between the TDSE solutions including either dipole or nondipole interaction of the electron with the radiation field. The evolution from the perturbative distribution at smaller k [Fig. 6(d) for $k = 1.7$] to the strongly nonperturbative regime [Fig. 6(a)] near $k = 1.83$ is clearly visible. The analytical model predicts the angular distribution reasonably well, with the largest deviations at $k = 1.80$ near the onset of strong destructive interference. For reference we also show in Fig. 6(a) the prediction by Pont *et al.* [4] for the angular distribution in the asymptotic high-field regime discussed above [Eq. (40)], which significantly differs from the present predictions for the intermediate-intensity regime.

Up to now, we have focused on the photoelectron angular distribution in the x-z plane (azimuthal angle $\varphi = 0$) perpendicular to the light propagation direction. Turning now to the y-z plane containing the propagation direction, we expect to find signatures of nondipole interactions [Eqs. (4) and (5)]. A direct comparison between the doubly differential distributions $P(k, \theta)$ in these two planes is given in Fig. 7. The additional magnetic force along the y direction that the electron experiences breaks the rotational symmetry about the z axis and leads to significant changes, which are most pronounced at large values of k. However, also for smaller values of k, the positions of the maxima and minima of the interference oscillations (along vertical cuts through Fig. 7) become θ dependent. This is a consequence of the angle dependence of the ac Stark shift [Eq. (44)]. Consequently, the interference oscillations are strongly damped in the angle-integrated spectrum (see Fig. 10 below). Nevertheless, the overall stabilization features are being kept intact in the y-z plane.

The angular distributions $P(k, \theta)$ in the y-z plane (i.e., $\varphi = \pi/2$; Fig. 8) display noticeable differences from those in the x-z plane (i.e., $\varphi = 0$). Even for relatively low k, deviations from a pure $\cos^2\theta$ distribution are evident. With increasing k the maximum shifts to larger angles. After a transient broadening (around $k = 1.8$ a.u.), the maximum shifts back to $\theta \approx 30^\circ$ at $k = 1.83$ a.u. The two alternative expressions for the nondipole interaction [Nd1 and Nd2, Eqs. (4) and (5)] yield nearly identical results for the angular distribution, indicating their approximate equivalence in the present parameter regime. The nondipole corrections within the semianalytical model reproduce the TDSE results quite well for low and high k values [Figs. 8(a), 8(c) and 8(d)]. Larger discrepancies can be found at intermediate values [Fig. 8(b)], although the qualitative trends are still accounted for. The simplified equation [Eq. (49)] applicable to the tails of the pulse ($t_2 \to \infty$)

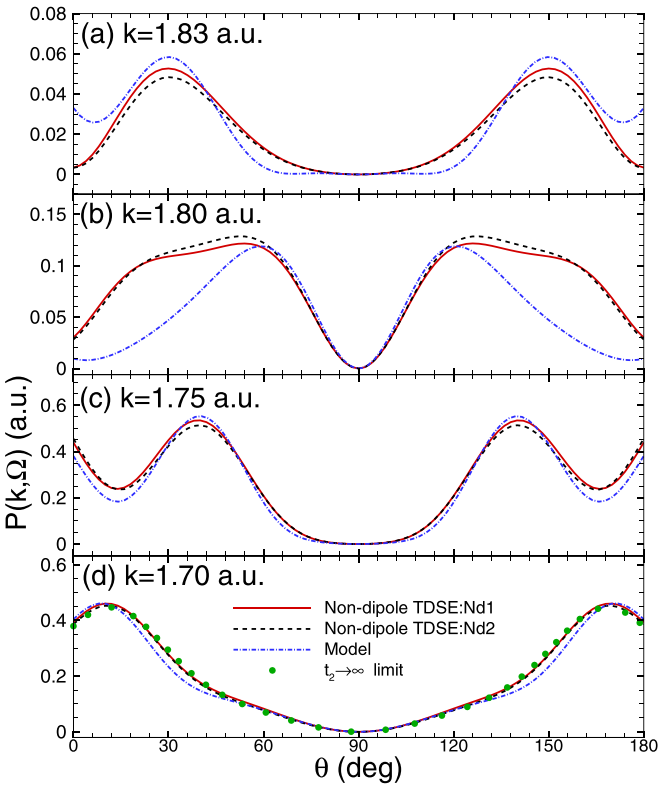

FIG. 8. Same as Fig. 6, but in the y-z plane ($k_y > 0$). The TDSE results employing two versions of nondipole corrections [Eqs. (4) and (5)] and the semi-analytical model [Eq. (41)] are shown. In (d), the result from the analytical equation [Eq. (49)] for the $t_2 \to \infty$ limit applicable to the tails is also shown (green dots).

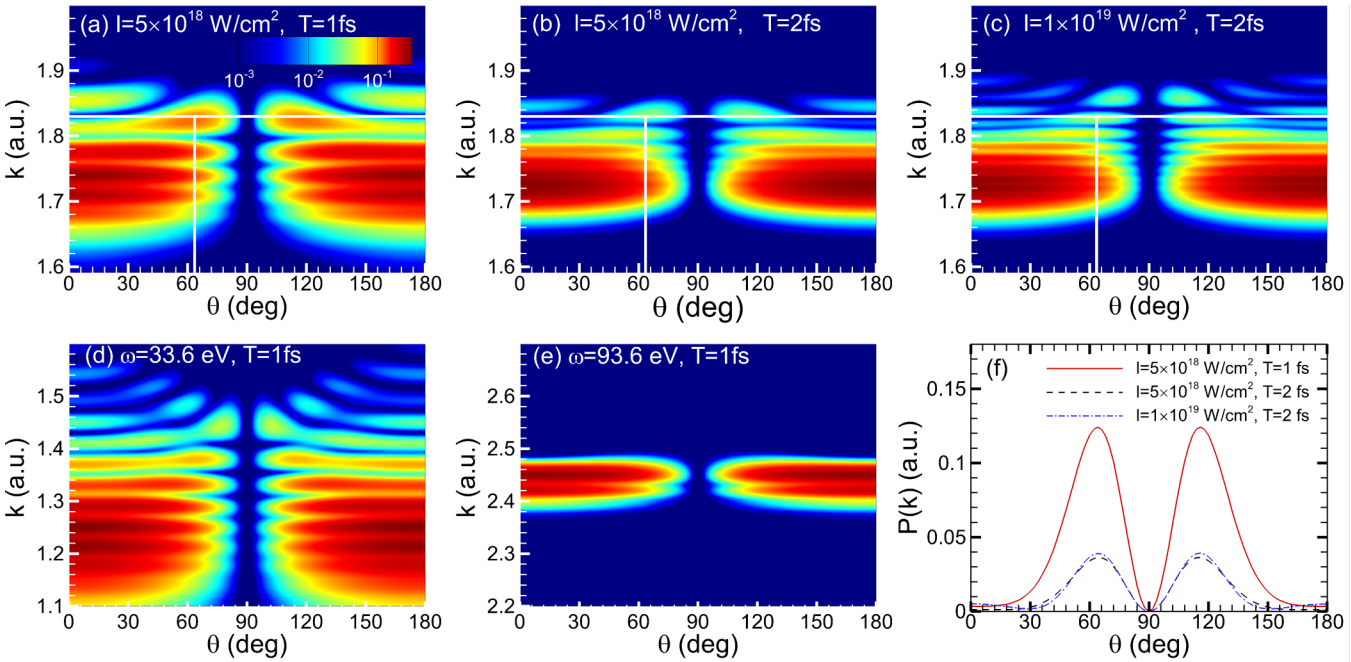

FIG. 9. Photoelectron momentum spectra for ionization of ground state of hydrogen. The pulse intensity is taken to be 5×10^{18} W/cm^2 in (a), (b), (d), and (e) and 1×10^{19} W/cm^2 in (c); the photon energy ω is taken to be 53.6 eV in (a)–(c). Other laser parameters are marked in each panel. The horizontal white lines in (a)–(c) mark the momentum $k = 1.83$ a.u., and $P(k)$ along this cut is shown in (f).

reproduces the angular distribution for the electrons ejected with low k ($k = 1.7$ a.u.) quite accurately.

Examples of the pulse-parameter dependence of the angular distributions in the stabilization regime are shown in Fig. 9. Qualitatively, the distributions in the (k-θ) plane remain unchanged. Increasing the pulse duration from 1 to 2 fs reduces the spacing between subsequent peaks of the dynamical interference oscillation [compare Figs. 9(a) and 9(b)] since a larger phase difference is accumulated between the emissions on the rising (t_1) and falling (t_2) edges. The shift of the maximum to large angles ($\theta \approx 63^\circ$) for large k is preserved. Decreasing the photon frequency [compare Figs. 9(a) and 9(d)] increases the number of observable oscillations within the linewidth because of the enhanced ac Stark shift. It furthermore shifts the maximum at high k values (here $k = 1.43$ a.u.) to larger angles ($\theta \approx 80^\circ$). Conversely, increasing ω [compare Figs. 9(a) and 9(e)] reduces the number of oscillations and renders the angular distribution more $\cos^2\theta$-like even for the highest values of k within the one-photon linewidth. This is a consequence of the reduced ac Stark shift for larger ω at fixed I. Furthermore, increasing the laser intensity [compare Figs. 9(b) and 9(c)] allows for the ejection of higher-energy photoelectrons. Although the interference features in the energy distribution are quite sensitive to the pulse length and intensity, the stabilization signatures in the angular distributions are rather stable. The angular distributions of the photoelectron at fixed energy are nearly identical [see Fig. 9(f)] for different pulse lengths and peak intensities. Since the stabilization signatures in the angular distributions will survive the temporal or spatial averaging over intensity, the conditions for their experimental observation appear to be quite favorable. The challenge is to reach peak intensities large enough to render a large phase amplitude $k_z\alpha_0$.

Finally, we present results for the angle-integrated photoelectron spectrum as a function of E (Fig. 10). The pronounced dynamical interference oscillations visible in dipole approximation are strongly damped when nondipole corrections are included. This is due to the fact that the nondipole correction induces an angle dependence of the energetic positions of the interference maxima (see Fig. 7). Integration over θ thus largely washed out the oscillations. However, the suppression of the high-energy tails due to the destructive interference (marked by a red arrow) caused by the rapidly varying quiver phase remains visible. Switching on the quiver phase ($k_z\alpha$) in the model strongly suppresses the peak at high energies (red arrow near $E = 46$ eV, $k = 1.83$ a.u.), effectively shifting the peak of the envelope over the oscillatory signal to lower energies ($E = 43$ eV, $k = 1.78$ a.u.). This shift closely mirrors the modification of the angular-differential spectrum by the destructive interference [Fig. 5(a)]. In the full TDSE the global interference phase cannot easily be switched off. However, its signature is still present in terms of a pronounced peak shift of the envelope to even lower energies ($E = 41$ eV, $k = 1.74$ a.u.). This peak position lies well below the anticipated value of $\omega + E_0 + \delta\bar{E}_0$ for photoionization of a Stark-shifted bound state.

V. SUMMARY

We have theoretically studied the stabilization effects in the angle-resolved photoelectron momentum spectra for ionization of a hydrogen atom by a single linearly polarized strong XUV laser pulse. We have focused on the transition regime of moderately strong, short XUV pulses with intensities of the order of 10^{18}-10^{19} W/cm^2, photon energies between 30 and 100 eV, and femtosecond pulse durations. This region

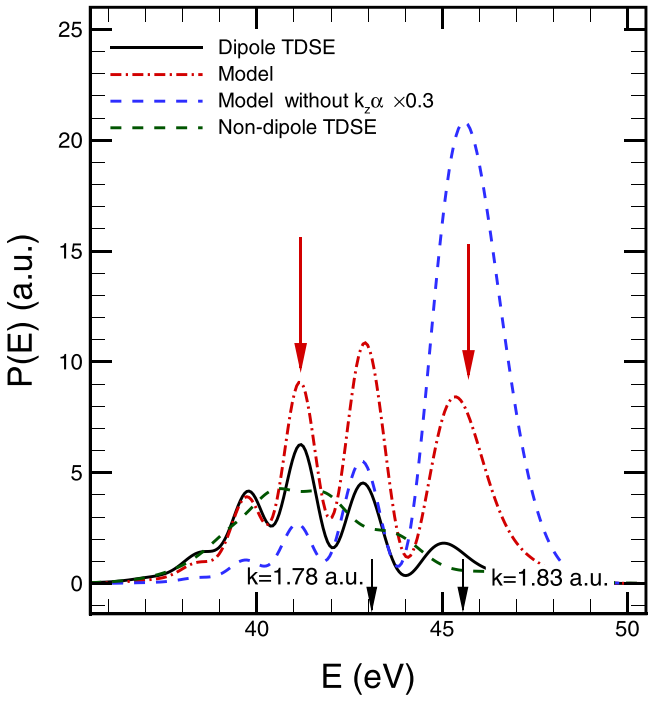

FIG. 10. Photoelectron energy spectra for ionization of the ground state of hydrogen. The laser pulse is the same as in Fig. 1. The predictions from TDSE calculations without (dipole TDSE) or with the nondipole correction (nondipole TDSE) are compared with the semianalytical model in the dipole approximation [Eq. (23)]. The energies corresponding to momenta $k = 1.78$ a.u. and $k = 1.83$ a.u. (see text) are indicated. The shift of the envelope peak is marked by two red arrows (compare with the blue dashed line).

is expected to become accessible with FEL and HHG light sources. Our present results predict strong stabilization effects on the angle-resolved photoelectron spectra. In this regime, stabilization was shown to be the consequence of destructive temporal interference between wave packets emitted at different instants of time acquiring a rapidly varying quiver phase. The temporal structure of the short XUV pulse plays an important role in the appearance of stabilization features. In this transition regime where the quiver amplitude is still comparable with the atomic diameter, the formation of a dichotomic wave function, the characteristic feature of stabilization in the high-field limit, is not yet well developed. We have developed a semianalytic model that reproduces features predicted by the numerical TDSE calculations quite well. It furthermore describes the departure of the angular distribution from that of the perturbative angular distribution $\propto \cos^2\theta$. It is modified and shifted to larger angles relative to the polarization axis. The variation of the cycle-averaged Stark shift during the strong XUV pulse was shown to be key to understand the stabilization process in this regime and to make a connection to high-field Floquet theories applicable for longer pulses. Stabilization features are much more prominently displayed at high instantaneous intensities, while they are absent in the tails of the pulse. They are also preserved when nondipole corrections to the electron-field interactions are included. Nondipole effects are very small for electrons ejected perpendicular to the laser propagation direction, making the predictions from the dipole approximation accurate in the plane perpendicular to the laser propagation direction. However, the nondipole correction results in a significant modification of the angular distribution in the plane containing the laser propagation vector. As a result, dynamical interference oscillations become strongly damped in the angle-integrated photoelectron spectra, while they are visible in the angular-differential spectrum.

ACKNOWLEDGMENTS

This work is supported by the National Natural Science Foundation of China (NSFC) (Grants No. 12074265, No. 11804233, No. 11747013, No. 11961131008, and No. 11725416), by the National Key R&D Program of China (Grant No. 2018YFA0306302), and by Grants No. FWF-SFB041-VICOM (Austria), No. FWF-SFB049-NEXTLITE (Austria), and No. FWF-W1243-SOLIDS4FUN (Austria) and COST action CA18234.

[1] M. Pont, N. R. Walet, M. Gavrila, and C. W. McCurdy, Dichotomy of the Hydrogen Atom in Superintense, High-Frequency Laser Fields, Phys. Rev. Lett. **61**, 939 (1988).

[2] M. Gavrila and J. Z. Kamiński, Free-Free Transitions in Intense High-Frequency Laser Fields, Phys. Rev. Lett. **52**, 613 (1984).

[3] M. Pont and M. Gavrila, Stabilization of Atomic Hydrogen in Superintense, High-Frequency Laser Fields of Circular Polarization, Phys. Rev. Lett. **65**, 2362 (1990).

[4] M. Pont, N. R. Walet, and M. Gavrila, Radiative distortion of the hydrogen atom in superintense, high-frequency fields of linear polarization, Phys. Rev. A **41**, 477 (1990).

[5] M. Pont, Atomic distortion and ac-Stark shifts of H under extreme radiation conditions, Phys. Rev. A **40**, 5659 (1989).

[6] M. Dörr, R. M. Potvliege, and R. Shakeshaft, Tunneling Ionization of Atomic Hydrogen by an Intense Low-Frequency Field, Phys. Rev. Lett. **64**, 2003 (1990).

[7] R. J. Vos and M. Gavrila, Effective Stabilization of Rydberg States at Current Laser Performances, Phys. Rev. Lett. **68**, 170 (1992).

[8] M. Pont, Multiphoton ionization in superintense, high-frequency laser fields. I. General developments, Phys. Rev. A **44**, 2141 (1991).

[9] M. Pont, Multiphoton ionization in superintense, high-frequency laser fields. II. Stabilization of atomic hydrogen in linearly polarized fields, Phys. Rev. A **44**, 2152 (1991).

[10] C. J. Joachain, N. J. Kylstra, and R. M. Potvliege, *Atoms in Intense Laser Fields* (Cambridge University Press, Cambridge, 2011).

[11] M. Gavrila, Atomic stabilization in superintense laser fields, J. Phys. B **35**, R147 (2002).

[12] J. H. Eberly and K. C. Kulander, Atomic stabilization by superintense lasers, Science **262**, 1229 (1993).

[13] *Atoms in Intense Laser Fields*, edited by M. Gavrila (Academic Press, San Diego, 1992).

[14] W. C. Henneberger, Perturbation Method for Atoms in Intense Light Beams, Phys. Rev. Lett. **21**, 838 (1968).

[15] M. P. de Boer, J. H. Hoogenraad, R. B. Vrijen, L. D. Noordam, and H. G. Muller, Indications of High-Intensity Adiabatic Stabilization in Neon, Phys. Rev. Lett. **71**, 3263 (1993).

[16] M. P. de Boer, J. H. Hoogenraad, R. B. Vrijen, R. C. Constantinescu, L. D. Noordam, and H. G. Muller, Adiabatic stabilization against photoionization: An experimental study, Phys. Rev. A **50**, 4085 (1994).

[17] N. J. van Druten, R. C. Constantinescu, J. M. Schins, H. Nieuwenhuize, and H. G. Muller, Adiabatic stabilization: Observation of the surviving population, Phys. Rev. A **55**, 622 (1997).

[18] B. Piraux and R. M. Potvliege, Adiabatic stabilization of a circular state: Theory compared to experiment, Phys. Rev. A **57**, 5009 (1998).

[19] U. Eichmann, A. Saenz, S. Eilzer, T. Nubbemeyer, and W. Sandner, Observing Rydberg Atoms to Survive Intense Laser Fields, Phys. Rev. Lett. **110**, 203002 (2013).

[20] U. Eichmann, T. Nubbemeyer, H. Rottke, and W. Sandner, Acceleration of neutral atoms in strong short-pulse laser fields, Nature (London) **461**, 1261 (2009).

[21] Q. Su, J. H. Eberly, and J. Javanainen, Dynamics of Atomic Ionization Suppression and Electron Localization in an Intense High-Frequency Radiation Field, Phys. Rev. Lett. **64**, 862 (1990).

[22] Q. Su and J. H. Eberly, Stabilization of a model atom in superintense field ionization, J. Opt. Soc. Am. B **7**, 564 (1990).

[23] Q. Su and J. H. Eberly, Suppression of ionization and atomic electron localization by short intense laser pulses, Phys. Rev. A **43**, 2474 (1991).

[24] L. You, J. Mostowski, and J. Cooper, Suppression of ionization in one- and two-dimensional-model calculations, Phys. Rev. A **45**, 3203 (1992).

[25] K. C. Kulander, K. J. Schafer, and J. L. Krause, Dynamic Stabilization of Hydrogen in an Intense, High-Frequency, Pulsed Laser Field, Phys. Rev. Lett. **66**, 2601 (1991).

[26] J. Grochmalicki, M. Lewenstein, and K. Rzążewski, Stabilization of Atoms in Superintense Laser Fields: Is It Real? Phys. Rev. Lett. **66**, 1038 (1991).

[27] F. Morales, M. Richter, S. Patchkovskii, and O. Smirnova, Imaging the Kramers–Henneberger atom, Proc. Natl. Acad. Sci. USA **108**, 16906 (2011).

[28] P.-L. He, Z.-H. Zhang, and F. He, Young's Double-Slit Interference in a Hydrogen Atom, Phys. Rev. Lett. **124**, 163201 (2020).

[29] M. Førre, S. Selstø, J. P. Hansen, and L. B. Madsen, Exact Nondipole Kramers-Henneberger form of the Light-Atom Hamiltonian: An Application to Atomic Stabilization and Photoelectron Energy Spectra, Phys. Rev. Lett. **95**, 043601 (2005).

[30] T. Birkeland, R. Nepstad, and M. Førre, Stabilization of Helium in Intense xuv Laser Fields, Phys. Rev. Lett. **104**, 163002 (2010).

[31] S. A. Sørngård, S. Askeland, R. Nepstad, and M. Førre, Multiphoton ionization and stabilization of helium in superintense xuv fields, Phys. Rev. A **83**, 033414 (2011).

[32] N. J. Kylstra, R. A. Worthington, A. Patel, P. L. Knight, J. R. Vázquez de Aldana, and L. Roso, Breakdown of Stabilization of Atoms Interacting with Intense, High-Frequency Laser Pulses, Phys. Rev. Lett. **85**, 1835 (2000).

[33] D. Bauer and F. Ceccherini, Electron correlation versus stabilization: A two-electron model atom in an intense laser pulse, Phys. Rev. A **60**, 2301 (1999).

[34] A. S. Simonsen and M. Førre, Magnetic-field-induced enhancement of atomic stabilization in intense high-frequency laser fields, Phys. Rev. A **92**, 013405 (2015).

[35] E. A. Seddon, J. A. Clarke, D. J. Dunning, C. Masciovecchio, C. J. Milne, F. Parmigiani, D. Rugg, J. C. H. Spence, N. R. Thompson, K. Ueda, S. M. Vinko, J. S. Wark, and W. Wurth, Short-wavelength free-electron laser sources and science: A review, Rep. Prog. Phys. **80**, 115901 (2017).

[36] B. W. J. McNeil and N. R. Thompson, X-ray free-electron lasers, Nat. Photon. **4**, 814 (2010).

[37] S. Huang, Y. Ding, Y. Feng, E. Hemsing, Z. Huang, J. Krzywinski, A. A. Lutman, A. Marinelli, T. J. Maxwell, and D. Zhu, Generating Single-Spike Hard X-Ray Pulses with Nonlinear Bunch Compression in Free-Electron Lasers, Phys. Rev. Lett. **119**, 154801 (2017).

[38] T. Ishikawa *et al.*, A compact x-ray free-electron laser emitting in the sub-angstrom region, Nat. Photon. **6**, 540 (2012).

[39] E. Allaria *et al.*, Control of the Polarization of a Vacuum-Ultraviolet, High-Gain, Free-Electron Laser, Phys. Rev. X **4**, 041040 (2014).

[40] *XFEL: The European X-Ray Free-Electron Laser. Technical Design Report*, edited by M. Altarelli *et al.* (DESY XFEL Project Group European XFEL Project Team Deutsches Elektronen-Synchrotron Member of the Helmholtz Association, Hamburg, Germany, 2006).

[41] M. Altarelli, The European x-ray free-electron laser facility in Hamburg, Nucl. Instrum. Methods Phys. Res. Sect. B **269**, 2845 (2011).

[42] M. W. Guetg, A. A. Lutman, Y. Ding, T. J. Maxwell, F.-J. Decker, U. Bergmann, and Z. Huang, Generation of High-Power High-Intensity Short X-Ray Free-Electron-Laser Pulses, Phys. Rev. Lett. **120**, 014801 (2018).

[43] M. Fuchs *et al.*, Anomalous nonlinear x-ray Compton scattering, Nat. Phys. **11**, 964 (2015).

[44] A. A. Sorokin, S. V. Bobashev, T. Feigl, K. Tiedtke, H. Wabnitz, and M. Richter, Photoelectric Effect at Ultrahigh Intensities, Phys. Rev. Lett. **99**, 213002 (2007).

[45] J. Liang, W.-C. Jiang, S. Wang, M. Li, Y. Zhou, and P. Lu, Atomic dynamic interference in intense linearly and circularly polarized XUV pulses, J. Phys. B **53**, 095601 (2020).

[46] S. Brennecke and M. Lein, High-order above-threshold ionization beyond the electric dipole approximation, J. Phys. B **51**, 094005 (2018).

[47] T. E. Moe and M. Førre, Ionization of atomic hydrogen by an intense x-ray laser pulse: An *ab initio* study of the breakdown of the dipole approximation, Phys. Rev. A **97**, 013415 (2018).

[48] M.-X. Wang, H. Liang, X.-R. Xiao, S.-G. Chen, W.-C. Jiang, and L.-Y. Peng, Nondipole effects in atomic dynamic interference, Phys. Rev. A **98**, 023412 (2018).

[49] M. Førre and A. S. Simonsen, Nondipole ionization dynamics in atoms induced by intense xuv laser fields, Phys. Rev. A **90**, 053411 (2014).

[50] M. Førre and A. S. Simonsen, Generalized velocity-gauge form of the light-matter interaction hamiltonian beyond the dipole approximation, Phys. Rev. A **93**, 013423 (2016).

[51] W.-C. Jiang and X.-Q. Tian, Efficient split-Lanczos propagator for strong-field ionization of atoms, Opt. Express **25**, 26832 (2017).

[52] T. N. Rescigno and C. W. McCurdy, Numerical grid methods for quantum-mechanical scattering problems, Phys. Rev. A **62**, 032706 (2000).

[53] M. J. Rayson, Lagrange-Lobatto interpolating polynomials in the discrete variable representation, Phys. Rev. E **76**, 026704 (2007).

[54] B. I. Schneider and L. A. Collins, The discrete variable method for the solution of the time-dependent Schrödinger equation, J. Non-Cryst. Solids **351**, 1551 (2005).

[55] X. M. Tong, K. Hino, and N. Toshima, Phase-dependent atomic ionization in few-cycle intense laser fields, Phys. Rev. A **74**, 031405(R) (2006).

[56] W.-C. Jiang and J. Burgdörfer, Dynamic interference as signature of atomic stabilization, Opt. Express **26**, 19921 (2018).

[57] W.-C. Jiang, X.-M. Tong, R. Pazourek, S. Nagele, and J. Burgdörfer, Theory of bound-state coherences generated and probed by optical attosecond pulses, Phys. Rev. A **101**, 053435 (2020).

[58] W.-C. Jiang, H. Liang, S. Wang, L.-Y. Peng, and J. Burgdörfer, Enhancing Autler-Townes splittings by ultrafast XUV pulses, Phys. Rev. Res. **3**, L032052 (2021).

[59] P. V. Demekhin and L. S. Cederbaum, Dynamic Interference of Photoelectrons Produced by High-Frequency Laser Pulses, Phys. Rev. Lett. **108**, 253001 (2012).

[60] P. V. Demekhin and L. S. Cederbaum, Coherent intense resonant laser pulses lead to interference in the time domain seen in the spectrum of the emitted particles, Phys. Rev. A **86**, 063412 (2012).

[61] W.-C. Jiang, S.-G. Chen, L.-Y. Peng, and J. Burgdörfer, Two-Electron Interference in Strong-Field Ionization of He by a Short Intense Extreme Ultraviolet Laser Pulse, Phys. Rev. Lett. **124**, 043203 (2020).

[62] P. V. Demekhin and L. S. Cederbaum, ac Stark effect in the electronic continuum and its impact on the photoionization of atoms by coherent intense short high-frequency laser pulses, Phys. Rev. A **88**, 043414 (2013).

[63] A. N. Artemyev, A. D. Müller, D. Hochstuhl, L. S. Cederbaum, and P. V. Demekhin, Dynamic interference in the photoionization of He by coherent intense high-frequency laser pulses: Direct propagation of the two-electron wave packets on large spatial grids, Phys. Rev. A **93**, 043418 (2016).

[64] M. Baghery, U. Saalmann, and J. M. Rost, Essential Conditions for Dynamic Interference, Phys. Rev. Lett. **118**, 143202 (2017).

[65] K. Toyota, O. I. Tolstikhin, T. Morishita, and S. Watanabe, Siegert-state expansion in the Kramers-Henneberger frame: Interference substructure of above-threshold ionization peaks in the stabilization regime, Phys. Rev. A **76**, 043418 (2007).

[66] K. Toyota, O. I. Tolstikhin, T. Morishita, and S. Watanabe, Interference substructure of above-threshold ionization peaks in the stabilization regime, Phys. Rev. A **78**, 033432 (2008).

[67] O. I. Tolstikhin, Siegert-state expansion for nonstationary systems. IV. Three-dimensional case, Phys. Rev. A **77**, 032712 (2008).